

On the Nitrogen-Induced Lattice Expansion of a Non-stainless Austenitic Steel, Invar 36[®], Under Triode Plasma Nitriding



XIAO TAO, ALLAN MATTHEWS, and ADRIAN LEYLAND

Chromium, as a strong nitride-forming element, is widely regarded to be an “essential” ingredient for the formation of a nitrogen-expanded lattice in thermochemical nitrogen diffusion treatments of austenitic (stainless) steels. In this article, a proprietary “chrome-free” austenitic iron-nickel alloy, Invar[®] 36 (Fe-36Ni, in wt pct), is characterized after triode plasma nitriding (TPN) treatments at 400 °C to 450 °C and compared with a “stainless” austenitic counterpart RA 330[®] (Fe-19Cr-35Ni, in wt pct) treated under equivalent nitriding conditions. Cr does indeed appear to play a pivotal role in colossal nitrogen supersaturation (and hence anisotropic lattice expansion and superior surface hardening) of austenitic steel under low-temperature (≤ 450 °C) nitrogen diffusion. Nevertheless, this work reveals that nitrogen-induced lattice expansion occurs below the nitride-containing surface layer in Invar 36 alloy after TPN treatment, implying that Cr is not a necessity for the nitrogen-interstitial induced lattice expansion phenomenon to occur, also suggesting another type of γ_N .

<https://doi.org/10.1007/s11661-019-05526-0>

© The Minerals, Metals & Materials Society and ASM International 2019

I. INTRODUCTION

AFTER early scientific studies published by Bell *et al.*^[1] and Ichii *et al.*^[2] in the 1980s, low-temperature plasma diffusion treatments have been widely investigated as a potential solution to the poor tribological performance of austenitic stainless steels (ASSs).^[3–7] Nitrogen-expanded austenite^[3] (γ_N ; also called “S-phase”^[2]) can be synthesized on ASSs (such as AISI 304, 310 and 316 type alloys, based mainly on the Fe-Cr-Ni ternary alloy system) under low-temperature (≤ 450 °C) nitriding without the formation of chromium nitride, where the original face-centered cubic (FCC) structure is expanded anisotropically under extremely high interstitial nitrogen uptake.^[8–10] Recent studies of expanded austenite (γ_N) have focused on the crystallographic structure of N-supersaturated ASS surfaces^[11–18]; however, there are still uncertainties about the roles of the primary substitutional alloying elements

(*e.g.*, Cr, Ni and/or Mn) in the formation of γ_N during low-temperature thermochemical diffusion treatment. This topic can be traced back to the 1990s, when authors such as Menthe *et al.*^[19] and Yasumaru^[20] reported that γ_N does not form in steels containing either Cr or Ni/Mn alone (*i.e.*, Fe-13Cr-0.2C, Fe-17Cr-0.1C, Fe-30Ni, Fe-32Ni, Fe-42Ni and Fe-26Mn-0.2C, in wt pct) under low-temperature nitriding. It was argued that both Cr and Ni/Mn are necessary for the formation of γ_N on austenitic steels. More recently however, Buhagiar *et al.*^[13] and Tao *et al.*^[18] reported the formation of γ_N on Ni-free high-Mn ASSs, proving unequivocally that neither Ni nor Mn is in itself crucial for the formation of γ_N (although each may affect differently the nitrogen supersaturation levels obtained, the lattice plasticity mechanisms and the γ_N lattice (in)stability observed with increasing treatment temperature/time^[18]).

On the other hand, Cr—as a strong nitride-forming element—is widely believed to be an “essential” component of the substrate alloy composition for γ_N formation (with appropriate mechanical/tribological/corrosion-resistant properties).^[21,22] Expanded austenite has been synthesized using various low-temperature nitrogen surface modification techniques on Fe/Ni/Co-based alloys with substrate Cr content ranging from ~ 13 at. pct (for proprietary precipitation hardening stainless steels, such as Nanoflex[®] and Corrax[®]^[23]) to ~ 31 at. pct (for a special Co-Cr alloy^[24]). A significant amount of Cr (as a “nitrogen trapper”) in the substrate (*i.e.*, ≥ 12 at. pct, also typical for stainless steels to promote the stable surface

XIAO TAO is with the Department of Materials Science and Engineering, The University of Sheffield, Sir Robert Hadfield Building, Mappin Street, Sheffield, S1 3JD, UK and also with the School of Metallurgy and Materials, University of Birmingham, Birmingham B15 2TT, UK. ALLAN MATTHEWS is with the School of Materials, The University of Manchester, Manchester, M13 9PL, UK. ADRIAN LEYLAND is with the Department of Materials Science and Engineering, The University of Sheffield. Contact e-mail: a.leyland@sheffield.ac.uk

Manuscript submitted April 26, 2019.

Article published online November 11, 2019

chromium oxide layer formation) appears to be important in the formation of “useful” γ_N under low-temperature nitrogen surface modification. The role of Cr has been investigated and discussed in several studies of γ_{N-304} and/or γ_{N-316} , which have pointed to “trapping and detrapping” diffusion of N^[25,26] and to the bonding (and short-range ordering) of N to Cr.^[19,27,28] It was postulated that Cr could provide trap sites for N, contributing to the extremely high interstitial absorption and anomalous (anisotropic) lattice expansion of ASSs, seen under low-temperature nitriding.^[10,22,28] Additionally, pure γ -Ni clearly shows no lattice expansion under nitrogen ion implantation,^[29,30] but γ_N was reported (with evident XRD peak shifts to lower 2θ angles) after nitrogen surface modification treatments on Ni-alloys that contain strong nitride formers, such as Ni-Cr binary alloys (containing ~ 20 at. pct Cr^[29,30] and ~ 26 at. pct Cr^[31]), Ni-Ti binary alloys (containing ~ 1.6 at. pct Ti,^[32] ~ 3.3 at. pct Ti^[32] and ~ 5.8 at. pct Ti^[31]) and a range of commercial Cr-containing Ni superalloys.^[29] While a (meta)stable austenitic substrate microstructure alone appears an insufficient requirement, strong nitride formers appear to be a necessity for the formation of γ_N on Fe/Ni/Co-based substrates.

Nevertheless, Williamson *et al.*^[29] reported “highly-expanded” and “less-expanded” FCC phases (designated as γ_{N1} and γ_{N2} , respectively, in their paper) on a Cr-free high-Ni Invar alloy (Fe-35Ni, in wt pct) after N implantation at 400 °C, which appears to be contradictory (and hence intriguing) to the widely reported “essential” role played by Cr in austenite lattice expansion under low-temperature nitrogen diffusion treatment. However, apart from surface XRD profiles, no further details were given in Reference 29 on the structure of expanded austenitic phases synthesized on Fe-35Ni. Alloy RA 330[®] (Fe-19Cr-35Ni, in wt pct), as a high-Ni stainless counterpart of Fe-35Ni Invar, was previously characterized by the authors of the present work after triode plasma nitriding (TPN).^[18] To investigate the γ_{N1} and γ_{N2} phases reported in Reference 29 and to elucidate the role of Cr, a TPN-treated non-stainless high-Ni austenitic steel, Invar 36[®] (Fe-36Ni, in wt pct), is investigated in this study and compared (under equivalent treatment conditions) with the TPN-treated alloy RA 330.

II. EXPERIMENTAL

The chemical compositions of Invar 36[®] (City Special Metals Ltd., Sheffield, UK) and RA 330[®] (Neonickel Ltd., Blackburn, UK) are presented in Table I. Disks of 20 mm diameter (and 3 mm thick) were sliced from a solution-annealed bar of alloy Invar 36 using an abrasive cutting wheel (Struers Secotom-50). Rectangular RA 330 alloy coupons of ~ 25 × 25 × 4 mm dimensions were cut from 4-mm-thick solution-annealed plates. Invar 36 samples were plasma nitrided in a modified commercial PVD coating unit, Tecvac IP70L, using a triode plasma nitriding (TPN) configuration^[3,33,34] under a treatment pressure of 0.4 Pa (with N₂:Ar gas volume ratio of 7:3) and substrate bias of

– 200 V, at 400 °C, 425 °C and 450 °C for 4 and 20 hours, respectively. The precise sample preparation and nitriding treatment procedures are described in detail in Reference 18.

A Nikon Eclipse LV150 optical microscope (OM) was used for optical imaging and a Philips XL30S FEG electron microscope (with Oxford Instruments INCA EDX system) for energy dispersive X-ray (EDX) spectroscopy. Beam acceleration voltage and spot size were 15 kV and 5, respectively. Beam intensity was calibrated with a cobalt standard before each measurement. The mean surface compositions were evaluated from ten random measurements over the material surface, where each measurement location covered an area of 65 × 45 μm^2 . Backscattered electron (BSE) images were taken from polished sample cross-sections using a FEI Nova NanoSEM 450 instrument at a beam acceleration voltage of 20 kV and spot size of 5.5. Vickers indentation hardness was evaluated using a Struers Durascan[®] 70 hardness tester. The indentation load and dwell time were 0.025 kg and 15 seconds, respectively. The mean surface hardness value, HV_{0.025}, was averaged from 12 randomly distributed indents. Nanoindentation hardness measurements were performed on polished sample cross sections using a Hysitron TriboScope[®] Nanoindenter (≤ 5 mN load, Berkovich diamond indenter). The displacements of indentations from the sample surface were measured *in situ* using an atomic force microscope attached to the nanoindenter. The mean hardness value at each depth level was averaged from five indentations.

X-ray diffraction analysis was performed at two-theta angles from 30 to 80 deg in Bragg-Brentano geometry using a Bruker D2 PHASER (30 kV, 10 mA, Cu-K α_{ave} 0.1542 nm) and in Seeman-Bohlin geometry at 2 deg glancing angle (GAXRD) using a PANalytical X’pert³ instrument (45 kV, 40 mA; monochromated CuK α_1 0.1541 nm). The 400 °C 20 hours nitrided and 450 °C 20 hours nitrided Invar samples were also ground using P1200 SiC paper to successively remove ~ 3/5/10/20/30 μm of the treatment layer (measured using a micrometer) and were examined respectively under GAXRD to determine the evolution of the phase structure with treatment depth. Cross-sectional thin foils for transmission electron microscopy (TEM) were prepared *via* focused ion beam (FIB) milling using an FEI Quanta 200 3D electron microscope with a 30-kV gallium ion beam attachment, as described previously.^[18] The thinned areas were examined under a Philips EM420 transmission electron microscope at a beam acceleration voltage of 120 kV. Scanning TEM (STEM) analysis was carried out using a FEI Philips Tecnai F20 electron microscope. STEM-EDX analysis was performed at 200 kV and a spot size of 6 (with Oxford Instruments AZtec EDX software).

III. RESULTS

A. Cross-sectional Backscattered Electron Images and Hardness-Depth Profiles

All nitrided Invar 36 surfaces show a discontinuous, feature-containing surface layer in Figure 1 (see

Table I. Material Composition (Weight Percent)

Material	Specification	Fe	Cr	Ni	Mn	C	Others
Invar 36 ^{®a}	ASTM F1686-06, UNS K93603	bal.	0.07	36.08	0.4	0.04	0.14 Si, 0.04 Co
RA 330 ^{®b}	ASTM B536-07 UNS N08330	bal.	18.5	34.9	1.4	0.05	0.16 Al, 0.14 Ti, 0.11 Cu, 1.2 Si, 0.01N

^aComposition of Invar 36[®] is presented according to the original material supplier Deutsche Nickel GmbH, and it also contains 0.032 wt pct (in total) of minor alloying additions of Al, Mg, Ti and Zr. The Ni content was confirmed using SEM-EDX.

^bComposition of RA 330[®] is presented according to the original material supplier ATI Allegheny Ludlum Corp.; the contents of major alloying elements (*i.e.*, Cr, Ni, Mn and Si) were confirmed using SEM-EDX.

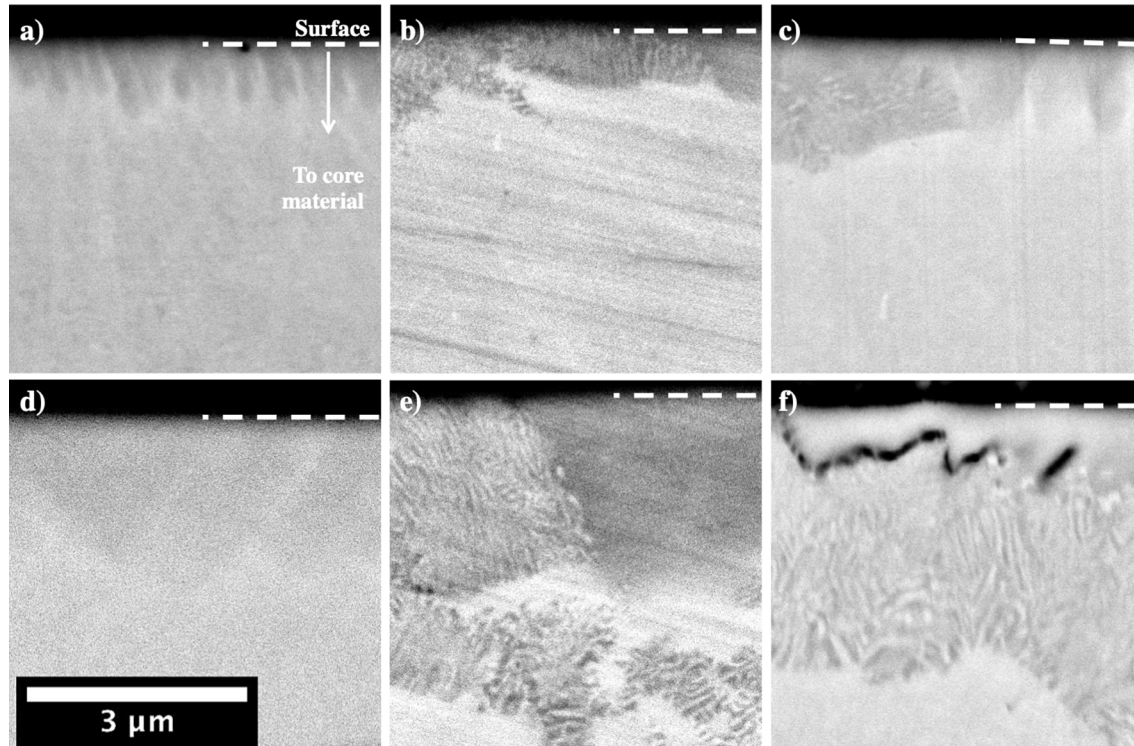


Fig. 1—Cross-sectional BSE images of Invar 36[®] after plasma nitriding at (a) 400 °C 4 h, (b) 425 °C 4 h, (c) 450 °C 4 h, (d) 400 °C 20 h, (e) 425 °C 20 h, (f) 450 °C 20 h.

Figure A1 in Appendix for BSE images of lower magnification). Neither the penetration depths nor the distributions of these features on nitrided Invar are homogeneous. At a treatment temperature of 400 °C, the dark features start forming from the very surface of material (Figure 1(a)) and then grow and coalesce with treatment time (Figure 1(d)). “Cellular” regions are observed in Invar 36 TPN treated at 425 °C and 450 °C. These cellular regions are composed of laminates of two different phases, with an interlamellar spacing of several tens of nanometers. Owing to the large discrepancy in atomic mass between interstitial nitrogen atoms and substitutional metal atoms (*i.e.*, 14 for N, 55.8 for Fe and 58.7 for Ni), the features observed on sample cross sections of Invar 36 under backscattered electron (BSE) imaging (Figure 1) mainly originate from the inhomogeneous distribution of nitrogen following TPN treatment. Under BSE imaging in Figure 1, lower mean atomic weight yields less electron scattering, so the

N-rich phase appears dark (and will be identified in the following Section III-C). It should also be mentioned that the black wavy features (in Figure 1(f)) are cracks, and this feature is clearly shown in the FIB-TEM sample in Section III-B.

The hardness-depth profiles of nitrided Invar (Figure 2(a)) indicate total case depths of ~11 and ~24 μm after treatments at 400 °C and 450 °C, respectively. Hardness profiles of nitrided Invar first drop steeply after leaving the nitride-containing surface layer and then gradually reduce as they approach the core. The hardened layers on nitrided Invar are clearly thicker than the feature-containing layers (observed in BSE images, Figures 1(d) and (f)) would suggest, and they correspond to deep nitrogen diffusion zones (see Section III-C).

In contrast, homogeneous γ_{N-330} layers were observed on alloy RA 330 after equivalent nitriding treatments.^[18] The hardened case depths on

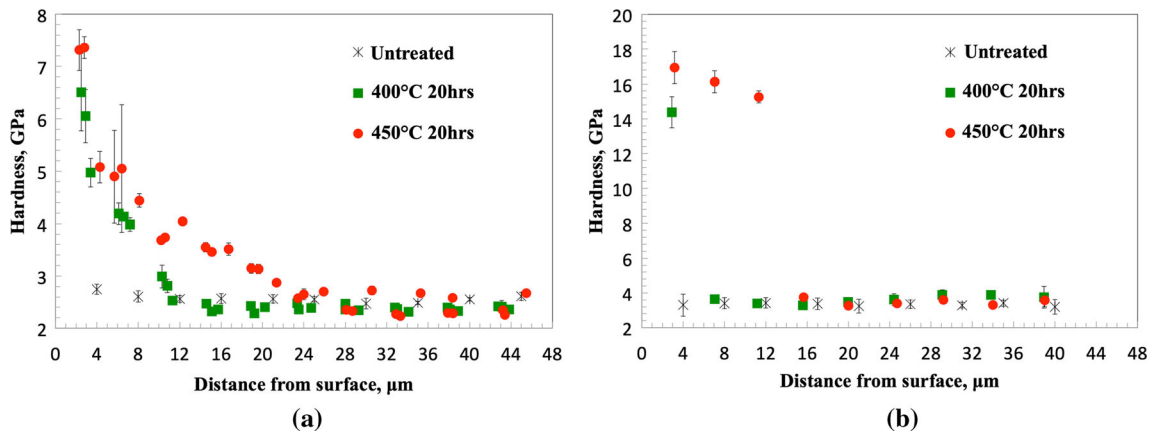


Fig. 2—Cross-sectional nanoindentation hardness-depth profiles of (a) Invar 36[®] and (b) RA 330[®] before and after TPN at 400 °C and 450 °C for 20 h (error bars— \pm 95 pct confidence interval at each depth level).

TPN-treated RA 330 in Figure 2(b) are consistent with the observed layer depths, *i.e.*, $\sim 4 \mu\text{m}$ at 400 °C and $\sim 14 \mu\text{m}$ at 450 °C.^[18] Compared with the hardness-depth profile of nitrified Invar (Figure 2(a)), γ_{N} -330 layers synthesized under equivalent treatment conditions are much harder (but significantly thinner) and present an abrupt drop in hardness at the layer/core interface (a characteristic feature of N-supersaturated austenite layers on stainless steel surfaces^[22,35]).

B. Phase Identification

1. XRD and GAXRD

The XRD profiles of nitrified Invar 36 in Figure 3(a) appear analogous to those reported for Invar 36 under nitrogen ion beam processing by Williamson *et al.*,^[29] showing “highly-expanded and less-expanded FCC structures” after treatment—where both expanded structures have an almost ideal FCC structure (as determined from the 111 and 220 peak positions). First, under both θ -2 θ XRD (Figure 3(a)) and GAXRD (Figure 3(b)), the peak positions of the “highly-expanded” FCC structure match with the $\text{Fe}_{4-x}\text{Ni}_x\text{N}$, PDF card 00-060-0479, stable for $0 < x < 3.3$ under experimental conditions^[36]. This highly expanded FCC structure (in Figure 3) could be identified as Fe_4N -type γ' -nitride. Different from the θ -2 θ XRD profiles of TPN-treated Invar (Figure 3(a)), the GAXRD profiles of the same materials (Figure 3(b)) reveal only the “highly expanded FCC” phase (*i.e.*, γ' -nitride) without the “less-expanded” FCC phase. Considering the shallow X-ray attenuation depth under GAXRD, γ' -nitride should correspond to a phase located close to the surface, with the “less-expanded” phase formed deeper in the diffusion zone. Then, the features observed in the near surface of nitrified Invar in Figure 1 can be attributed to the formation of γ' -nitride. Additionally, an unexpanded γ (111) peak (near 43.5 deg) is also seen on Invar after 20 hours treatment at 425 °C and 450 °C (Figure 3), which can be closely correlated with the (bright) N-depleted lamellae in the “cellular” region.

To reveal the surface phases on nitrified Invar (typically, the “less-expanded FCC structure”) that contribute to deep hardened zones in Figure 2(a), the 400 °C 20 hours and 450 °C 20 hours nitrified Invar samples were further investigated under GAXRD before and after successive layer removal, as shown in Figure 4. The γ' peaks were observed on both samples to a depth of $\sim 3 \mu\text{m}$. At a depth of $\sim 3 \mu\text{m}$, unexpanded γ peaks were evident on Invar after TPN for 20 hours at 450 °C, but are not observed after 20 hours treatment at 400 °C. These unexpanded γ peaks at $\sim 3 \mu\text{m}$ depth on the 450 °C and 20 hours treated Invar alloy appear to correspond to the bright N-depleted lamellar phase in the “cellular” region in Figure 1(f).

More importantly, below the γ' -containing surface zones, the “less-expanded FCC structure” is clearly revealed at depths from ~ 3 to $20 \mu\text{m}$ with continuous XRD peak shifts to higher 2θ angles from surface to core (toward the peak positions of substrate austenite, as indicated by red arrows in Figure 4), until the unmodified core is reached at a depth of $\sim 30 \mu\text{m}$. The “less-expanded FCC structure,” γ_{N} -Invar, appears to be continuously expanded from the parent austenite under the insertion of interstitial nitrogen. The gradual shift of γ_{N} -Invar peaks to higher 2θ angles with increasing depth could be attributed to the commensurate reduction of nitrogen in solid solution from surface to core, which also leads to a gradually reducing hardness with depth in the γ_{N} -Invar regions (Figure 2(a)).

2. FIB-TEM

Cross-sectional TEM samples of 400 °C and 450 °C 20 hours nitrified Invar surfaces were also prepared and investigated. Extra “forbidden” FCC spots are revealed for γ' (Figures 5(b1, 2) and (e)), but not for γ_{N} -Invar (Figures 5(c1, 2)), in good agreement with the weak γ' (110) GAXRD peaks observed in Figure 3(b). At a treatment temperature of 400 °C, the topmost γ' is revealed under DF-TEM imaging using γ' (110) diffraction electrons in which γ' appears slightly brighter than the underlying γ_{N} -Invar (Figure 5(a)). This topmost γ' -nitride shares the same crystal orientation as the underlying γ_{N} -Invar, with a cubic-to-cubic

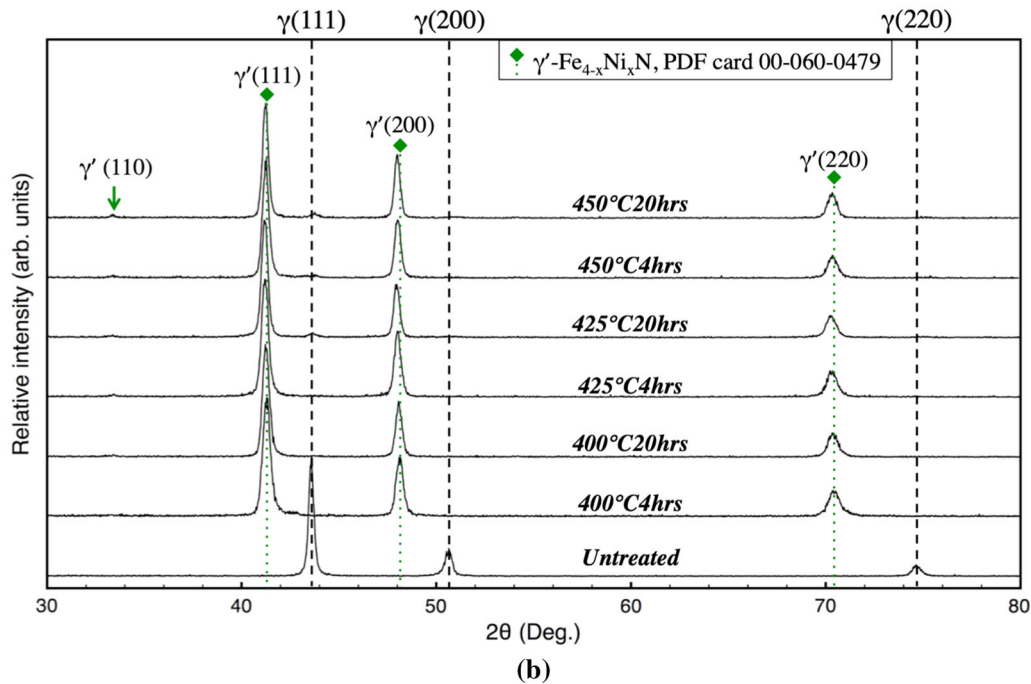
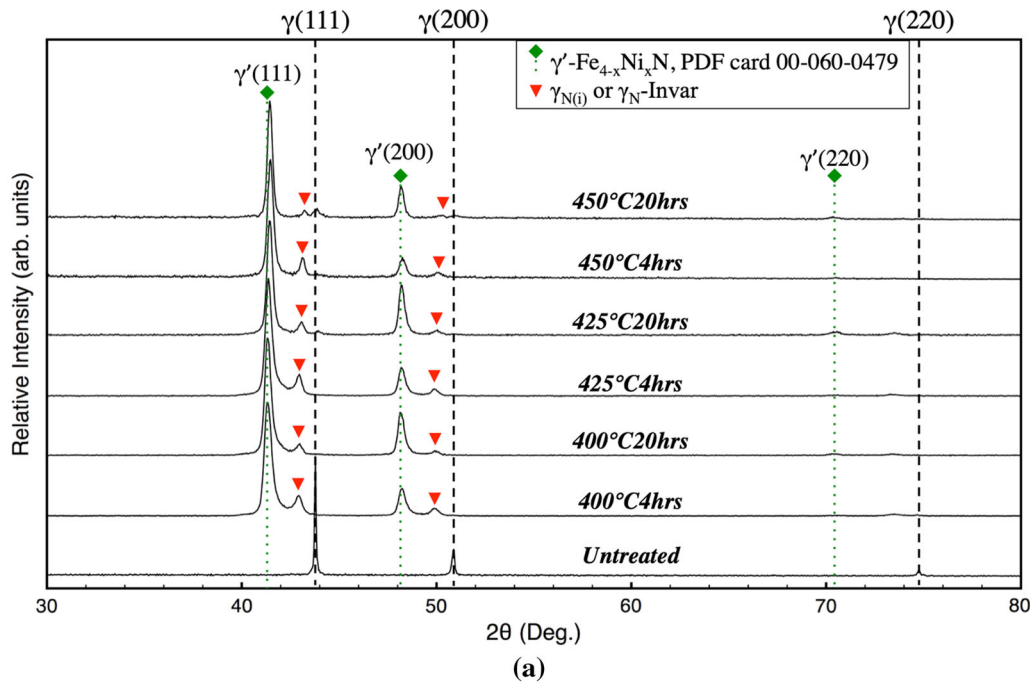


Fig. 3—(a) Theta-2theta XRD and (b) GAXRD profiles of TPN-treated Invar 36[®].

structure-orientation relationship, in which case γ' appears to transform from γ_N -Invar *via* interstitial-nitrogen ordering (into an Fe_4N -type structure) during TPN.

There are different colonies of phase mixtures in the intermediate cellular regions on 450 °C and 20 hours TPN-treated Invar. The selected area EDP of a colony (*i.e.*, the dark region in the middle of Figure 5(d)) presents two sets of FCC diffraction spots (Figure 5(e)), suggesting a cubic-to-cubic orientation relationship and

a lattice parameter ratio of ~ 1.05 (as determined from electron diffraction distances) between the two phases. Taking one of the phases in the phase mixture as being γ' -nitride (lattice parameter of 0.3789 nm, PDF card 00-060-0479), the lattice parameter of the other FCC phase can be estimated as ~ 0.3609 nm, which is very close to the lattice parameter of ~ 0.3606 nm measured for untreated austenite, as determined by the 111 peak positions from GAXRD profiles in Figure 4. Together with the γ' and unexpanded XRD peaks observed for

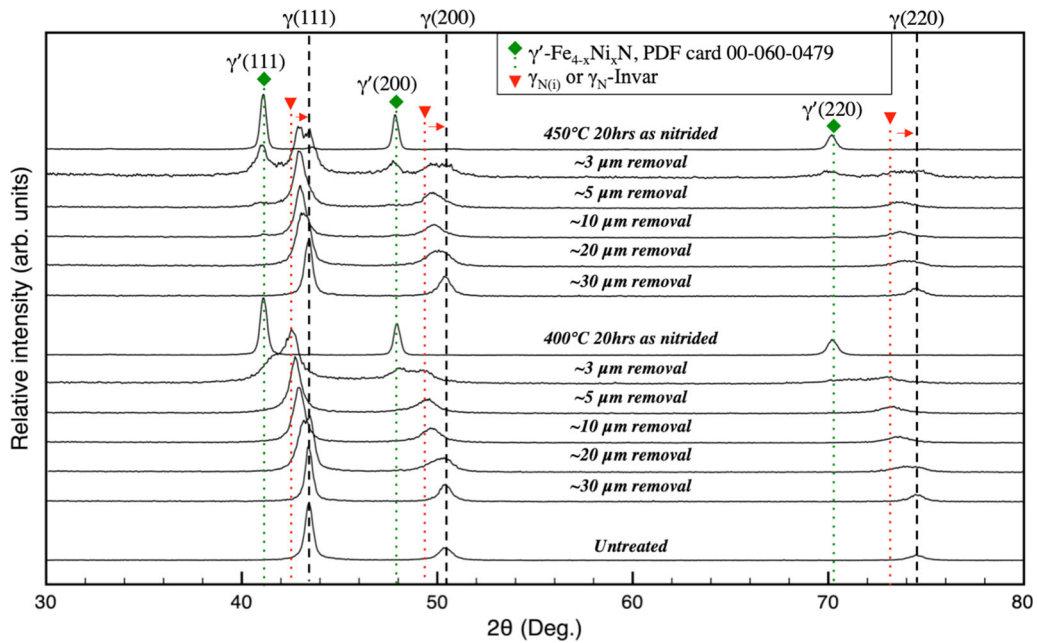


Fig. 4—GAXRD profiles of the 400 °C 20 h and the 450 °C 20 h nitrided Invar 36® before and after successive layer removal compared with the untreated sample.

the 450 °C TPN-treated Invar at $\sim 3 \mu\text{m}$ depth in Figure 4, the phase mixture appears to be γ' and unexpanded γ . These colonies of phase mixtures do not share the same crystal orientation to each other. No consistent crystallographic relation was observed between the colony of the phase mixture in Figure 5(d) and the underlying (and probably the parent) γ_{N} -Invar. The formation of these phase mixtures is likely to occur *via* nucleation and growth of γ' . Additionally, cracks are observed and indicated with white arrows in Figure 5(d). This micro-cracking is believed to be associated with the formation of γ' .

Furthermore, the lamellar phase mixture on Invar nitrided at 450 °C and 20 h can clearly be seen in HAADF imaging (Figure 6(a)). STEM-EDX analysis of the phase mixture (Figure 6) indicates redistribution of both interstitial nitrogen and substitutional metallic elements (*e.g.*, Fe with Ni). Compared with the adjacent N-depleted regions, the N-rich regions exhibit higher Fe content (Figure 6(b)) but lower Ni content (Figure 6(c)). Given that γ' -Fe $_{4-x}$ Ni $_x$ N is stable for $0 < x < 3.3$,^[36] the γ' formed in cellular regions have different compositions (*i.e.*, much lower Ni content) from those uniform γ' phases that formed *via* interstitial ordering (probably γ' -Fe $_{2.6}$ Ni $_{1.4}$ N, at $x \approx 1.4$ considering 35 at. pct Ni). The high-Ni γ phase (adjacent to low-Ni γ') could still contain a very small amount of residual nitrogen, such that the γ phase in the cellular region has a different composition from γ -Invar—and could therefore possess a different lattice parameter. Thus, the phase mixture in cellular regions could be attributed to local eutectoid decomposition of γ_{N} -Invar to an intimate mixture of lamellar low-Ni γ' and high-Ni, low-nitrogen γ . Additionally, minor alloying elements (such as Cr, Mn, Si, Co and C, see Table I) could also re-distribute between the two phases in this cellular region; however, probably

owing to their low concentrations, such re-distribution was not clearly visible in the EDX analysis (see for example Cr in Figure 6(e)).

C. Surface Nitrogen Content and Hardness

Surface nitrogen contents of nitrided Invar samples (Table II) ranged from ~ 18 to ~ 20 at. pct, which is significantly higher than the maximum equilibrium N-solubility limit in γ -Fe (*i.e.*, ~ 10.3 at. pct at ~ 650 °C^[37]), but lower than the surface nitrogen content of the nitrided alloy RA 330 (ranging from ~ 23 to 26 at. pct).^[18] The presence of Cr in the austenitic lattice of alloy RA 330 does appear to be beneficial in obtaining a higher surface nitrogen uptake. Surface N content of the Invar samples does not vary significantly with treatment temperature and time, which could be attributed to the formation of γ' nitride at the substrate surface.

Both alloys exhibit significant hardening after TPN treatment (Table II), and the hardening effect increases with treatment temperature and/or time. Maximum Vickers surface hardness was achieved at the upper treatment condition (of 450 °C for 20 hours) for both alloys. The hardness values obtained are influenced by different factors, such as the nitrogen composition-depth profile, phase distribution, indent penetration depth and nitride layer depth. The increase in surface hardness for TPN-treated Invar with treatment temperature and time could be attributed to: (1) the growth of a diffusion zone, (2) the development of uniform γ' -Fe $_{2.6}$ Ni $_{1.4}$ N phase at the material surface and (3) the lamellar phase mixtures that contain fine lamella of low-Ni γ' and high-Ni (low-N) γ . Owing to the colossal nitrogen supersaturation, alloy 330 generally possesses significantly higher surface hardness compared with Invar

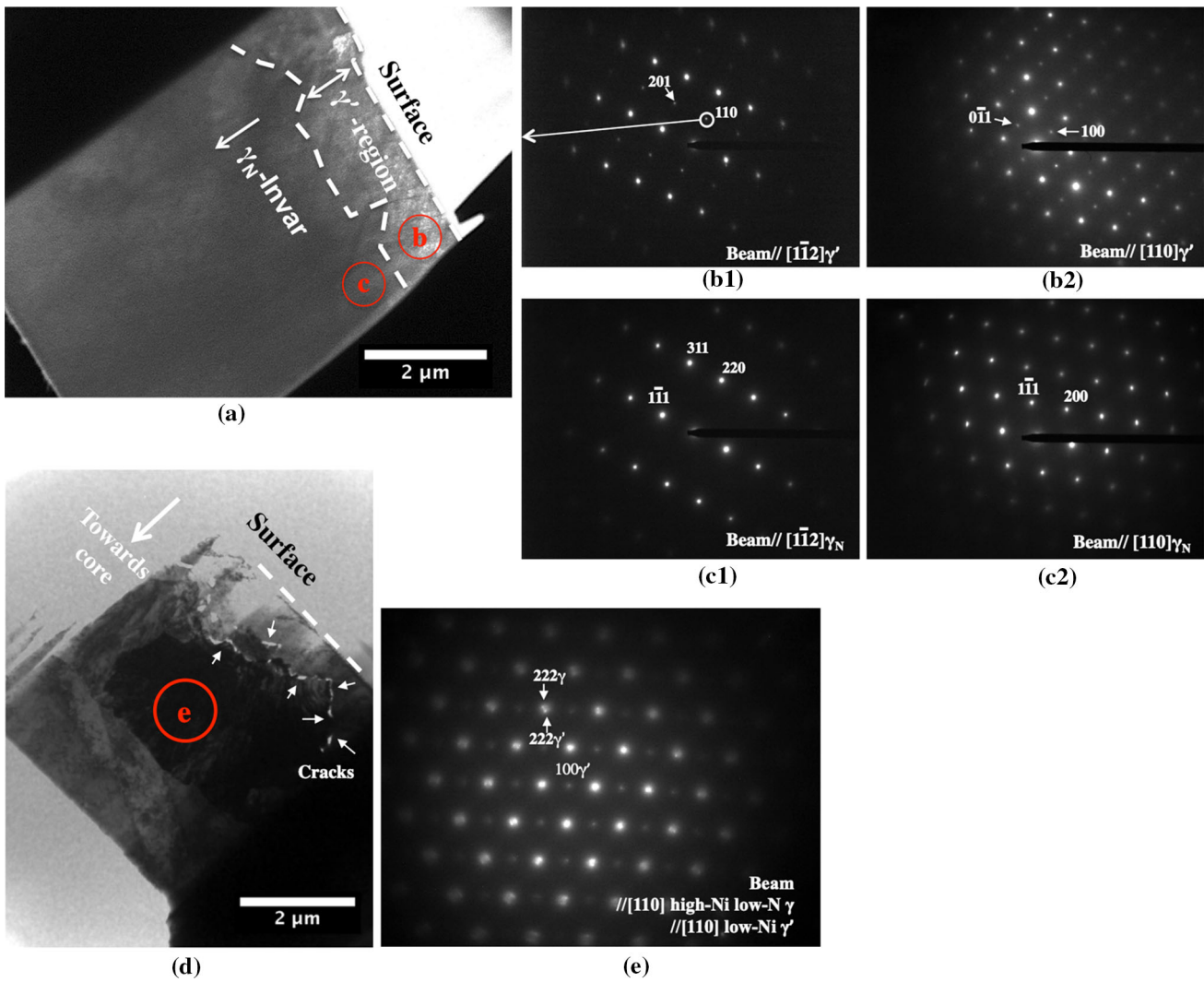


Fig. 5—(a) DF-TEM image of 400 °C 20 h nitrided Invar, constructed with 110 γ' diffraction electrons as indicated in Fig. 6(b1); (b1, 2) SAEDs of region b; (c1, 2) SAEDs of region c; (d) BF-TEM image of 450 °C 20 h nitrided Invar; (e) SAED of region e.

Table II. Surface Nitrogen Content and Hardness

	Surface At. Pct Nitrogen Invar 36 [®]	Surface Hardness, HV _{0.025}	
		Invar 36 [®]	RA 330 [®]
Untreated	—	200 ± 3	210 ± 4
400 °C 4 h	18.3 ± 0.4	390 ± 5	520 ± 10
400 °C 20 h	19.8 ± 0.3	498 ± 8	1048 ± 62
425 °C 4 h	18.9 ± 0.3	531 ± 8	515 ± 17
425 °C 20 h	20.6 ± 0.3	705 ± 25	1494 ± 21
450 °C 4 h	18.8 ± 0.6	638 ± 8	786 ± 26
450 °C 20 h	19.6 ± 0.6	734 ± 12	1573 ± 18

Values of surface nitrogen content and layer depths are shown as mean ± 95 pct confidence interval; surface nitrogen contents of nitrided RA 330[®] were shown in Ref. [18].

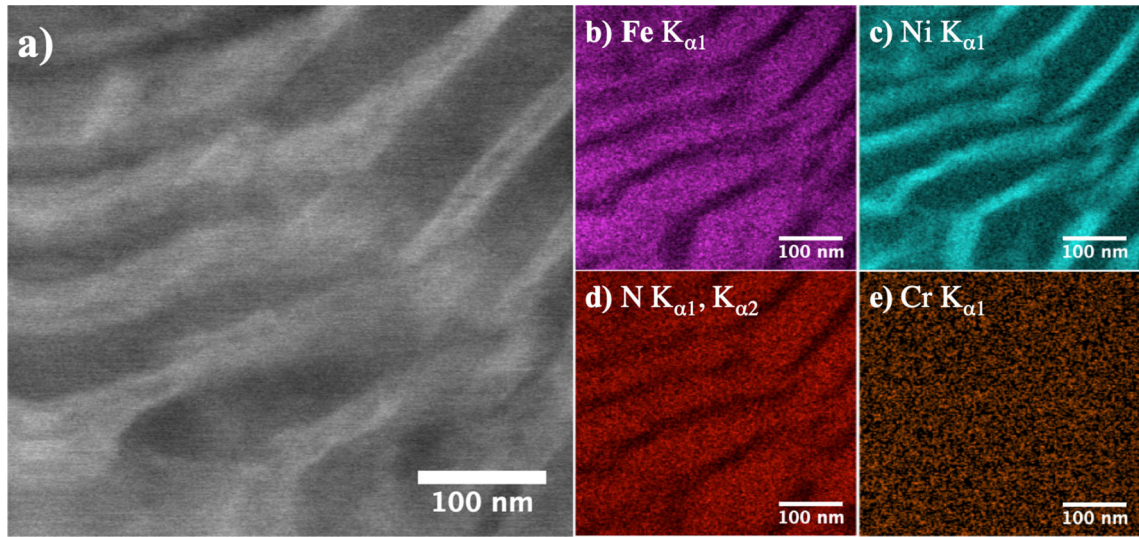


Fig. 6—(a) HAADF image showing the lamellar phase mixture; STEM-EDX maps of the region for (b) Fe ($K_{\alpha 1}$), (c) Ni ($K_{\alpha 1}$), (d) N ($K_{\alpha 1}$ and $K_{\alpha 2}$) and (e) Cr ($K_{\alpha 1}$).

under equivalent treatment conditions, although the nitrified layers on alloy 330 tend to be thinner than those on Invar after an equivalent TPN treatment.

IV. DISCUSSION

A. Interstitial Nitrogen Absorption and Lattice Expansion

In this study, γ_N denotes the entire group of nitrogen-expanded austenites, with specific phase notation based on the substrate material, such as γ_N -Invar, γ_N -330 and γ_N -316 (formed on Invar 36, alloy RA 330 and AISI 316 ASS, respectively). Comparisons between the γ_N -Invar in this study and the γ_N -330 in Reference 18 reveal that having a significant amount of Cr in the substrate does appear to be conducive to obtaining extremely high levels of interstitial nitrogen incorporation, but is at the same time not a necessity for the nitrogen-induced lattice expansion phenomenon to occur. The γ_N -Invar observed could be classified as $\gamma_{N(i)}$ [*i.e.*, where (i) signifies an absence of strong-nitride-formers in the substrate alloy composition], while the widely reported interstitial nitrogen-supersaturated and (typically strongly anisotropic) expanded austenite synthesized on Cr-containing ASSs could be denoted as $\gamma_{N(ii)}$. Noticeably, the commercial Invar 36[®] alloy employed in this study still contains ~ 0.7 wt pct Cr (and ≤ 0.032 wt pct of Al + Mg + Ti + Zr, see Table I), while the Fe-35Ni Invar steel substrate used in Reference 29 (where γ_N -Invar was also synthesized) was reported only to contain minor Si content (*i.e.*, ~ 1 at. pct of Mn + Si + C).

The terminology of “expanded austenite” was originally introduced to describe austenites with expanded lattice parameters (after nitrifying treatments) over those for nitrogen-containing austenite at maximum equilibrium solubility.^[38] After the re-definition of “heavily strained austenite” for this terminology,^[3] the expanded austenite terminology is now typically used to denote the interstitially supersaturated (and anisotropically expanded) austenites generally investigated and reported in the field of surface engineering.^[39] Nevertheless, expanded austenite, taking the literal meaning of the terminology, includes both $\gamma_{N(i)}$ and $\gamma_{N(ii)}$. With there being no (or much lower amounts of) “nitrogen trappers” in γ_N -Invar, the route by which $\gamma_{N(i)}$ forms appears to be different from the “nitrogen trapping” in $\gamma_{N(ii)}$. The ability to accommodate interstitial nitrogen in the parent FCC matrix (with a lattice expansion) typically at non-equilibrium conditions (*i.e.*, low treatment temperatures) arguably depends on the “chemical environment” (or, as suggested by Dong,^[22] the electronic structure) provided by the parent alloy with respect to the interstitial species (*e.g.*, N or C atoms) rather than simply the presence of a significant amount of Cr (or another strong-nitride-former).

Interstitial supersaturation is a known (and probably the most essential) feature for $\gamma_{N(ii)}$. As for γ_N -Invar, there is a lack of information on the equilibrium N solubility in γ -Invar, and there is still a question as to whether the γ_N -Invar obtained is N-supersaturated or dissolves nitrogen below the equilibrium solubility limit. Nitrogen solubility in Fe-Ni alloys is known to decrease as Ni content increases.^[40] According to the partial isothermal section of Fe-Ni-N at 700 °C,^[36] the equilibrium nitrogen solubility drops from ~ 10 at. pct in γ -Fe

to ~ 1 at. pct in γ -(Fe, 35Ni). Thus, it is anticipated that the equilibrium nitrogen solubility in γ -Invar will be much lower than that in “pure” γ -Fe (*i.e.*, ~ 10.3 at. pct N at ~ 650 °C^[37]). Nevertheless, the lattice parameters for γ _N-Invar (~ 0.364 nm at 450 °C and up to ~ 0.368 nm at 400 °C, measured from the 111 γ _N-Invar peak positions at ~ 3 μ m depth in Figure 4) are very close to those of γ -Fe with nitrogen at maximum equilibrium solubility (estimated as ~ 0.365 nm, using $0.3572 + [0.00078 \times \text{at. pct N}]$ from Reference 41). Given such substantial lattice expansion, the γ _N-Invar obtained is likely N-supersaturated (and could be metastable). However, further study is still required to establish precisely the chemical composition (especially the upper limit of nitrogen solvation) of γ _N-Invar and to understand the thermodynamic properties of Fe-Ni-N, typically with Ni content close to ~ 35 at. pct Ni and at temperatures < 450 °C.

Owing to the different interstitial absorption, one other significant difference between γ _{N(i)} and γ _{N(ii)} is their lattice expansions observable under XRD. The XRD peak shifts (to lower 2θ angles with respect to substrate peak positions) of γ _N-Invar are much smaller than those of γ _N-330 after equivalent thermochemical treatments. More importantly, anomalous (anisotropic) lattice expansion, where the XRD peak shift appears significantly larger for 200 reflections than with other hkl planes, is a known signature for the γ _{N(ii)} synthesized on ASSs under low-temperature nitriding^[7,11,17] (as observed also for γ _N-330^[18]). Compared with γ _{N(ii)}, γ _N-Invar exhibits a seemingly “isotropic” lattice expansion—where the observed 111 and 200 XRD peak shifts appear similar after nitrogen insertion (Figure 3)—for non-stainless austenitic steels under low-temperature nitrogen diffusion treatment. However, taking the GAXRD peak positions (from Figure 4) of substrate γ -Invar and the γ _N-Invar at a depth of ~ 5 μ m, the lattice expansions measured for the 111 and 200 XRD reflections are (1) ~ 1.6 and ~ 1.8 pct, respectively, at 400 °C and 20 hours and (2) ~ 1.1 and ~ 1.2 pct, respectively, at 450 °C and 20 hours. γ _N-Invar also deviates from an ideal FCC structure, but this deviation appears much less pronounced for γ _N-Invar, presumably owing to the much lower nitrogen absorption levels. This “slightly distorted FCC structure” of γ _N-Invar could be attributed mainly to the effect of elastic anisotropy of the FCC lattice (with a small compressive stress state) under N-induced lattice expansion. The γ _N-Invar layer synthesized under ion implantation for 15 min by Williamson *et al.*^[29] is much thinner than the γ _N-Invar layers synthesized under TPN in this study, where the θ - 2θ XRD profile of the former covers the entire γ _N-Invar layer and the abovementioned expansion anisotropy was not clearly observed. Furthermore, an “expanded FCC” phase has been reported on alloy 330 after hot ammonia corrosion at 500 °C for 1540 hours,^[42] which was presumed to be a nitrogen-containing iron-nickel phase (after the formation of Cr nitride) that may be a phase similar to γ _N-Invar. However, given the white monolayer shown in cross section after etching and the absence of CrN under XRD examination of the “corroded” alloy 330,^[42] the

“expanded FCC” phase on alloy 330 is suspected to be γ _N-330 and probably therefore the first explicit example of γ _{N(ii)} published (in 1961) in the open journal literature.

Last but not the least, the “less expanded FCC structure” on Invar (Fe-35Ni, in Reference 29) can now be identified as γ _{N(i)}, being a Cr-free N-expanded austenite. However, Ni-20Fe,^[29] Fe-30Ni, Fe-32Ni, Fe-42Ni and some FCC Fe-Mn-C steels^[19,20]—also having a Cr-free FCC substrate structure (based on the Fe-Ni or Fe-Mn-C system)—showed only a thin γ' layer without γ _{N(i)} under low-temperature nitriding treatments (or nitrogen ion implantation). Nevertheless, detailed structural/compositional information was not provided for the nitrified non-stainless austenitic steels in References 19, 20 and 29. Thick γ' surface layers might exist, such that underlying nitrogen-containing metallic phase(s) were not revealed by XRD. It may be worthwhile to re-visit these alloys (typically the Fe-Ni binary steels with Ni content close to ~ 35Ni wt pct) under low-temperature thermochemical diffusion treatments. If γ _{N(i)} forms only for certain substrate compositions, further study may be required on the electronic structure, bonding states and/or magnetic properties of γ _N-Invar to elucidate the mechanisms of its formation.

B. Decomposition of γ _N

Given the cubic-to-cubic crystallographic orientation relationship between γ' and γ _N-Invar seen after nitriding at 400 °C (Figures 5(a) through (c)), the formation of Fe₄N-type γ' in γ _N-Invar could be realized *via* diffusion and ordering of the interstitial nitrogen, without the need for substitutional diffusion. At elevated treatment temperatures, eutectoid decomposition occurs in γ _N-Invar under segregation of substitutional elements (Figure 6). The cellular decomposition morphology of γ _N-Invar appears similar to that of decomposed γ _N-316.^[43] Nevertheless, decomposition products of γ _N-Invar in the cellular regions are Fe₄N-type $\gamma' + \gamma$, whereas for γ _N-316 they are CrN + γ .

One signature feature of γ _{N(ii)} is its metastability under paraequilibrium conditions, where the low diffusivity of substitutional elements (*e.g.*, Fe, Cr and Ni) hinders the lattice decomposition mechanisms associated with CrN formation. After TPN at 400 °C, no evidence of CrN was found in γ _N-330,^[18] whereas γ' forms in γ _N-Invar *via* interstitial ordering. At slightly higher treatment temperatures (*i.e.*, 425 °C and 450 °C), the substitutional diffusion-facilitated decomposition occurs more readily in Cr-free γ _N-Invar compared with γ _N-330. Although γ _{N(i)} (*e.g.*, γ _N-Invar) may exhibit significantly lower nitrogen solvency and lattice expansion than γ _{N(ii)} (*e.g.*, γ _N-330), the former appears thermodynamically less stable. In this case, Cr atoms in γ _{N(ii)} assist in stabilizing the N-rich and expanded FCC structure by (1) providing Cr-N type bonding that competes with Fe-N type bonding and (2) providing an extremely slow lattice decomposition mechanism at the low treatment temperatures employed. Future investigations could be performed to address the as yet unanswered questions as to (1) how much “nitrogen

trapper” is required in the substrate alloy composition for the onset of $\gamma_{N(ii)}$ formation after thermochemical diffusion treatment and (2) whether other strong nitride-forming elements could replicate the role of (or replace) Cr in obtaining $\gamma_{N(ii)}$ on austenitic steel substrates. Furthermore, addition of strong nitride-forming elements other than Cr could inhibit the formation of CrN in $\gamma_{N(ii)}$ and push the thermal stability of $\gamma_{N(ii)}$ to a higher treatment temperature,^[44] in which case austenitic metallic substrates alloyed with combinations of strong nitride-forming elements (*e.g.*, Cr, Al, Ti and/or Nb; each element to no more than a few weight percent) may possess superior thermodynamic stability upon nitrogen supersaturation, enabling higher treatment/service temperature of nitrogen-expanded austenite.

C. Nitrogen Interstitial Diffusion

Comparing the surface nitrogen contents and the hardness-depth profiles between Invar 36 (Figure 2(a)) and alloy RA 330 (Figure 2(b)) after TPN treatment, nitrogen atoms were retained at the surface and distributed more homogeneously in the relatively thin diffusion layers of $\gamma_{N(ii)}$. However, the high level of Cr content in stainless steel substrates, while promoting lattice interstitial supersaturation (and thus a superior hardening response), appears also to impede significantly nitrogen inward diffusion, possibly owing to the trapping and detrapping diffusion kinetics proposed in Reference 26. Noticeably, the Invar 36 substrate contains minor additions of strong nitride formers (*e.g.*, Cr, Al, Ti and Zr, in total $< \sim 0.1$ wt pct), which could influence the nitrogen diffusion rate in Invar 36. There should be a threshold concentration level of the strong nitride former (or combinations thereof) in austenitic steel, above which interstitial diffusion in the austenite matrix slows down and nitrogen atoms are retained at the surface owing to the “trap effect.”

Comparing thermochemical diffusion treatments of AISI 316 ASS by nitrogen (γ_{N-316}) or carbon (γ_{C-316}) in the literature (the alloy for which probably the most extensive prior published data exists), γ_{N-316} layers possess composition-depth profiles with a high nitrogen plateau followed an abrupt drop in nitrogen content at the diffusion layer front (with corresponding lattice expansions and hardness/depth profiles),^[35,45,46] while the carbon concentration (and corresponding lattice expansion and hardness) in γ_{C-316} layers is normally lower, with a smoothly reducing depth profile toward the substrate core.^[8,45–47] Examining chemically homogeneous γ_{C-316} and γ_{N-316} powders, carbon absorption of γ_{C-316} ranges from 0 to ~ 18 at. pct,^[48,49] while γ_{N-316} has been shown to possess a higher limit of interstitial nitrogen solvation (*e.g.*, ~ 14 to 38 at. pct N^[10]) and, unlike carbon, also a lower limiting value. For the $\gamma_{N-Invar}$ zones observed in this study, the continuous lattice expansion from the unmodified core

(Figure 4) and the smoothly reducing hardness-depth profiles (Figure 2(a)) hint at there being no lower interstitial solvation limit for nitrogen in this alloy—and the smoothly reducing nitrogen depth profile appears very different from γ_{N-316} (but somewhat similar to γ_{C-316}). The abovementioned differences between γ_{N-316} (as a type of $\gamma_{N(ii)}$) and $\gamma_{N-Invar}$ (as a type of $\gamma_{N(i)}$), which could be associated with the strong chemical affinity between Cr and N, confirm the influence of the “chemical environment” of the substrate alloy (*e.g.*, with or without Cr) on the absorption of interstitial N during thermochemical diffusion treatment.

D. Nitrogen Interstitial Ordering

Compared with FCC- γ , one distinctive feature of γ' is the nitrogen interstitial ordering, where the “inserted” N atoms occupy the body centers, *i.e.*, $\frac{1}{2}\frac{1}{2}\frac{1}{2}$, of the host FCC cubes. Such interstitial ordering gives rise to the extra “forbidden” FCC reflections in EDPs (compare Figures 5(b1, 2) and (c1, 2)) and the $\gamma'(110)$ peak under XRD (Figure 3(b)). These extra diffraction reflections are also widely observed for $\gamma_{N(ii)}$ layers, reported under both electron diffraction (*e.g.*, in γ_{N-316} ,^[50,51] γ_{N-304} ^[52] and γ_{N-AG17} ^[18]) and XRD (*i.e.*, γ_{N-316} ^[53]). These reflections are not observed in $\gamma_{N(ii)}$ when the nitrogen content is low^[18,51] and are only observed under XRD when the nitrogen content is extremely high (*i.e.*, for the “chemically homogeneous” γ_{N-316} powders containing ~ 35.5 at. pct N^[53]). With increasing nitrogen content, $\gamma_{N(ii)}$ could show (1) no forbidden FCC reflections (at low N content), (2) forbidden reflections under electron diffraction (potentially owing to nitrogen interstitial ordered domains^[51] at intermediate-to-high N content) and (3) forbidden reflections under X-ray diffraction (owing to long-range ordering of interstitial nitrogen^[53] under extreme conditions of high N uptake). More importantly, Cr-containing Fe₄N-like γ' phases^[54] were reported in the $\gamma_{N(ii)}$ formed on Fe-Cr-Ni alloys, typically at the topmost surface (with the highest nitrogen concentration). The Cr-containing Fe₄N-like γ' in $\gamma_{N(ii)}$ is somewhat comparable to the uniform Cr-free Fe₄N-type γ' in $\gamma_{N(i)}$ as both of them could form *via* interstitial diffusion and/or ordering of nitrogen at low treatment temperature. In this regard, $\gamma_{N(ii)}$ could exhibit a random solid solution of N, short-range-ordering of N or long-range-ordering of N, depending on the local nitrogen concentration. The exact location of interstitial N in $\gamma_{N(ii)}$ is so far unclear and should vary at different stages of nitrogen absorption level, but probably N atoms are “trapped” at octahedral interstices near substitutional Cr atoms in the FCC unit cell. In contrast, the $\gamma_{N(i)}$ in this study does not present extra “forbidden” diffraction signals either under electron diffraction or by XRD, *i.e.*, there is no evidence of any

interstitial ordering. A Fe-Ni-N solid solution is anticipated for $\gamma_{N(i)}$, with nitrogen atoms randomly occupying some fraction of the octahedral interstices.

V. CONCLUSIONS

Further to a previous study on the role of Mn and Ni in the formation and structure of nitrogen-expanded austenite on ASSs, another (and arguably more important) aspect, i.e., the role of Cr in the formation of γ_N (and/or on the alloy selection/design criteria for nitrogen interstitially expandable steels/alloys), is discussed in the present work. Compared with the anisotropic nitrogen-expanded austenite $\gamma_{N(ii)}$ (e.g., γ_N -330 that formed on 330 alloy), an almost isotropic nitrogen-expanded austenite $\gamma_{N(i)}$ (viz. γ_N -Invar) is revealed on a non-stainless austenitic steel (Invar 36[®]) after TPN treatment, showing very different lattice expansion and surface-hardening behavior. Cr-alloying in austenitic steel substrates is an important factor in obtaining colossal nitrogen interstitial supersaturation, but the occurrence of interstitial-induced lattice expansion under low temperature nitrogen thermochemical diffusion treatment does not require a significant content of Cr in the substrate.

The γ_N -Invar diffusion zones, although providing less of a hardening effect, are much thicker than those on γ_N -330. Comparing the decomposition between γ_N -330 and γ_N -Invar, the presence of Cr alloying appears beneficial in suppressing the formation of γ' -Fe₄N type iron nitrides and enhancing the thermodynamic stability of γ_N . This implies a need for further study on the contents of nitride-forming elements required in austenitic alloys (and/or austenite-containing duplex or precipitation-hardening alloys) to effectively “trap” interstitial N atoms for optimum nitrogen absorption during low-temperature diffusion treatment (i.e., to maximize—and stabilize— γ_N formation, while retaining high nitrogen interstitial inward diffusion rates for hard and thick treatment layers). For example, austenitic metallic matrices (such as Ni or Fe-Ni/Mn) alloyed with (combinations of) strong nitride-forming elements could be evaluated under different low-temperature nitriding conditions to explore the optimal balance between treatment efficiency and treatment layer stability.

ACKNOWLEDGMENTS

This research did not receive any specific Grant from funding agencies in the public, commercial, or not-for-profit sectors. We would however like to thank City Special Metals Ltd. (Sheffield, UK) for the provision of alloy Invar[®] 36 for this study.

APPENDIX

See Figure A1.

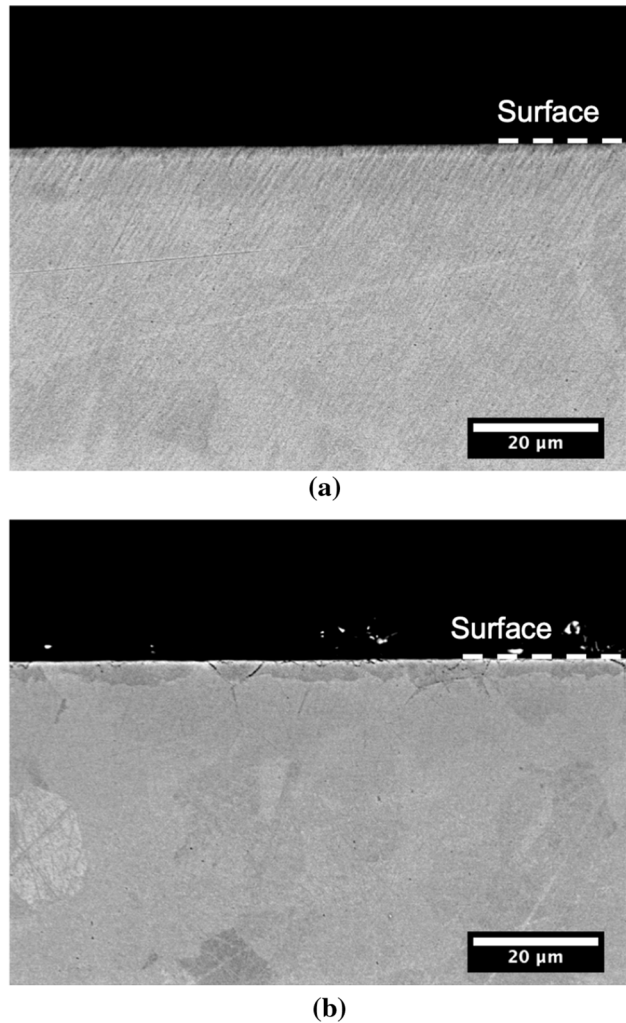


Fig. A1—Cross-sectional BSE images of Invar 36[®] after plasma nitriding at (a) 400 °C and (b) 450 °C for 20 h at a low magnification to cover the entire hardened zones. No clear features were found corresponding to γ_N -Invar. The “grain structure” observed probably results from different BS electron scattering behaviors at different grain orientations.

REFERENCES

1. Z.L. Zhang and T. Bell: *Surf. Eng.*, 1985, vol. 1, pp. 131–36.
2. K. Ichii, K. Fujimura, and T. Takase: *Technol. Rep. Kansai Univ.*, 1986, vol. 27, pp. 135–44.
3. A. Leyland, D.B. Lewis, P.R. Stevenson, and A. Matthews: *Surf. Coat. Technol.*, 1993, vol. 62, pp. 608–17.
4. D.B. Lewis, A. Leyland, P.R. Stevenson, J. Cawley, and A. Matthews: *Surf. Coat. Technol.*, 1993, vol. 60, pp. 416–23.
5. A. Matthews and A. Leyland: *Mater. Sci. Forum*, 1994, vols. 163–165, pp. 497–508.
6. Y. Sun and T. Bell: *Wear*, 1998, vol. 218, pp. 31–42.
7. Y. Sun, X.Y. Li, and T. Bell: *J. Mater. Sci.*, 1999, vol. 34, pp. 4793–4802.
8. Y. Cao, F. Ernst, and G.M. Michal: *Acta Mater.*, 2003, vol. 51, pp. 4171–81.
9. S. Collins and P. Williams: *Advanced Materials and Process*, ASM International, Cleveland, 2006, pp. 32–33.
10. T. Christiansen and M.A.J. Somers: *Metall. Mater. Trans. A*, 2006, vol. 37A, pp. 675–82.
11. T. Christiansen and M.A.J. Somers: *Scripta Mater.*, 2004, vol. 50, pp. 35–37.
12. T. Christiansen and M.A.J. Somers: *Z. Metallkd.*, 2006, vol. 97, pp. 79–88.

13. J. Buhagiar, X. Li, and H. Dong: *Surf. Coat. Technol.*, 2009, vol. 204, pp. 330–35.
14. J.C. Stinville, P. Villechaise, C. Templier, J.P. Riviere, and M. Drouet: *Acta Mater.*, 2010, vol. 58, pp. 2814–21.
15. C. Templier, J.C. Stinville, P. Villechaise, P.O. Renault, G. Abrasonis, J.P. Riviere, A. Martinavicius, and M. Drouet: *Surf. Coat. Technol.*, 2010, vol. 204, pp. 2551–58.
16. F.A.P. Fernandes, T.L. Christiansen, G. Winther, and M.A.J. Somers: *Acta Mater.*, 2015, vol. 94, pp. 271–80.
17. B.K. Brink, K. Stahl, T.L. Christiansen, J. Oddershede, G. Winthiner, and M.A.J. Somers: *Scripta Mater.*, 2017, vol. 131, pp. 59–62.
18. X. Tao, X. Liu, A. Matthews, and A. Leyland: *Acta Mater.*, 2019, vol. 164, pp. 60–75.
19. E. Menthe, K.T. Rie, J.W. Schultze, and S. Simsson: *Surf. Coat. Technol.*, 1995, vols. 74–75, pp. 412–16.
20. N. Yasumaru: *Mater. Trans. JIM*, 1998, vol. 39, pp. 1046–52.
21. D.L. Williamson, I. Ivanov, R. Wei, P.J. Wilbur: *Mater. Res. Soc. Symp. Proc.*, 1992, vol. 235.
22. H. Dong: *Int. Mater. Rev.*, 2010, vol. 55, pp. 65–98.
23. R.B. Frandsen, T. Christiansen, and M.A.J. Somers: *Surf. Coat. Technol.*, 2006, vol. 200, pp. 5160–69.
24. J. Lutz, J.W. Gerlach, and S. Mandl: *Phys. Status Solidi A*, 2008, vol. 205, pp. 980–84.
25. D.L. Williamson, J.A. Davis, P.J. Wilbur, J.J. Vajo, R. Wei, and J.N. Matossian: *Nucl. Instrum. Methods Phys. Res. Sect. B*, 1997, vols. 127–128, pp. 930–34.
26. S. Parascandola, W. Moller, and D.L. Williamson: *Appl. Phys. Lett.*, 2000, vol. 76, pp. 2194–96.
27. J.P. Riviere, M. Cahoreau, and P. Meheust: *J. Appl. Phys.*, 2002, vol. 91, pp. 6361–66.
28. J. Oddershede, T.L. Christiansen, K. Stahl, and M.A.J. Somers: *Scripta Mater.*, 2010, vol. 62, pp. 290–93.
29. D.L. Williamson, J.A. Davis, and P.J. Wilbur: *Surf. Coat. Technol.*, 1998, vols. 103–104, pp. 178–84.
30. F. Pedraza, C. Savall, G. Abrasonis, J.P. Riviere, J.F. Dinhut, and J.L. Grosseau-Poussard: *Thin Solid Films*, 2007, vol. 515, pp. 3661–69.
31. T. Makishi and K. Nakata: *Metall. Mater. Trans. A*, 2004, vol. 35A, pp. 227–38.
32. M. Fonovic, A. Leineweber, O. Robach, A. Jagle, and E.J. Mittemeijer: *Metall. Mater. Trans. A*, 2015, vol. 46A, p. 4115.
33. A. Leyland, K.S. Fancey, A.S. James, and A. Matthews: *Surf. Coat. Technol.*, 1990, vol. 41, pp. 295–304.
34. A. Leyland, K.S. Fancey, and A. Matthews: *Surf. Eng.*, 1991, vol. 7, pp. 207–15.
35. M.A.J. Somers and T. Christiansen: in *Thermochemical Surface Engineering of Steels*, E.J. Mittemeijer and M.A.J. Somers, eds., Woodhead Publishing, Cambridge, 2015, 1st ed., pp. 581–614.
36. P. Perrot: in *Landolt-Bornstein - Group IV Physical Chemistry (Numerical Data and Functional Relationships in Science and Technology)*, G. Effenberg and S. Ilyenko, eds., Springer, Berlin, Heidelberg, 2008, vol. 11D, Part 4.
37. H.A. Wriedt, N.A. Gokcen, and R.H. Nafziger: *Bull. Alloy Phase Diagrams*, 1987, vol. 8, p. 355.
38. S.P. Hannula and O. Nenonen: *Thin Solid Films*, 1989, vol. 181, pp. 343–50.
39. M.A.J. Somers and T. Christiansen: Low temperature surface hardening of stainless steel in *Thermochemical Surface Engineering of Steels*, E.J. Mittemeijer and M.A.J. Somers, eds., Woodhead Publishing, Cambridge, 2015, 1st ed., pp. 557–79.
40. D. Atkinson and C. Bodsworth: *J. Iron Steel Inst. Lond*, 1970, vol. 208, pp. 587–93.
41. D.H. Jack and K.H. Jack: *Mater. Sci. Eng.*, 1973, vol. 11, pp. 1–27.
42. J.J. Moran, J.R. Mihalisin, and E.N. Skinner: *Corrosion*, 1961, vol. 17, pp. 191t–95t.
43. X.Y. Li and Y. Sun: Transmission electron microscopy study of S phase in low temperature plasma nitrided 316 stainless steel in *Stainless Steel 2000: Thermochemical Surface Engineering of Stainless Steel*, T. Bell and K. Akamatsu, eds., Maney Publishing, London, 2001, 1st ed., pp. 215–28.
44. T. Christiansen, K.L. Dahm, and M.A.J. Somers: *BHM Berg- und Hüttenmännische Monatshefte*, 2015, vol. 160, pp. 406–12.
45. T. Christiansen and M.A.J. Somers: *Surf. Eng.*, 2005, vol. 21, pp. 445–55.
46. S. Thaiwatthana, X.Y. Li, H. Dong, and T. Bell: *Surf. Eng.*, 2002, vol. 18, pp. 433–37.
47. G.M. Michal, F. Ernst, H. Kahn, Y. Cao, F. Oba, N. Agarwal, and A.H. Heuer: *Acta Mater.*, 2006, vol. 54, pp. 1597–1606.
48. T.L. Christiansen, K. Stahl, B.K. Brink, and M.A.J. Somers: *Steel Res. Int.*, 2016, vol. 87, pp. 1395–1405.
49. T.S. Hummelshøj, T.L. Christiansen, and M.A.J. Somers: *Scripta Mater.*, 2010, vol. 63, pp. 761–63.
50. D. Stroz and M. Psoda: *J. Microsc.*, 2010, vol. 237, pp. 227–31.
51. J.C. Jiang and E.I. Meletis: *J. Appl. Phys.*, 2000, vol. 88, pp. 4026–31.
52. K. Tong, F. Ye, H. Che, M.K. Lei, S. Miao, and C. Zhang: *J. Appl. Crystallogr.*, 2016, vol. 49, pp. 1967–71.
53. B.K. Brink, K. Stahl, T. Christiansen, C. Frandsen, M.F. Hansen, and M.A.J. Somers: *Acta Mater.*, 2016, vol. 106, pp. 32–39.
54. H.L. Che, S. Tong, K.S. Wang, M.K. Lei, and M.A.J. Somers: *Acta Mater.*, 2019, vol. 177, pp. 35–45.

Publisher's Note Springer Nature remains neutral with regard to jurisdictional claims in published maps and institutional affiliations.